High-temperature X-ray Diffraction Measurements of Fluorite-Related Rare Earth Antimonates Ln_3SbO_7 (Ln = Nd, Tb) and Their Magnetic Properties

Yukio Hinatsu* and Yoshihiro Doi

Division of Chemistry, Graduate School of Science, Hokkaido University, Sapporo 060-0810, Japan

*tel/fax: +81-11-706-2702

email:hinatsu@sci.hokudai.ac.jp

Keywords: Magnetic properties; Rare earth; Oxides; Specific heat, Defect-fluorite

Abstract

Ternary rare-earth antimonates Ln_3SbO_7 (*Ln* = rare earths) were prepared, and their structures were determined by X-ray diffraction measurements. They crystallize in an orthorhombic superstructure of cubic fluorite (space group *Cmcm* for *Ln* = La, Pr; *Ccmm* for *Ln* = Sm - Dy), in which Ln^{3+} ions occupy two different crystallographic sites (the 8-coordinated and 7-coordinated). For *Ln* = Nd, two phases with the *Cmcm* and *Ccmm* space groups coexist at room temperature. When the temperature was increased, the Nd_3SbO_7 compound transformed into a single phase with the space group *Cmcm*. Through magnetic susceptibility measurements, an antiferromagnetic transition was observed at 3.0 K (*Ln* = Nd) and 7.8 K (*Ln* = Tb). Analysis of the magnetic specific heat for Tb_3SbO_7 indicates that the 8-coordinated Tb ions magnetically orders at 7.8 K, and with furthermore decreasing temperature, the 7-coordinated Tb ions shows antiferromagnetic ordering at 3.0 K.

1. Introduction

Metal oxides of the general formula Ln_3MO_7 (Ln = lanthanides, *M* = Nb, Mo, Ru, Sb, Ta, Re, Os, Ir) have been extensively studied. They have a defect-fluorite structure. The relationship to the fluorite structure is as follows. The fluorite unit cell for oxides has the composition $M^{4+}{}_4O_8$. If the four tetravalent metal ions are replaced by three trivalent ions (*Ln*) and one pentavalent ion (*M*), one oxide vacancy is formed per fluorite cell. Due to the significant differences in radii between the Ln^{3+} and M^{5+} ions, cation ordering occurs on the metal sites and the oxide-vacancy orders on the anion sites.

In 1979, Rossell first determined the crystal structure for La_3NbO_7 [1]. It is well described in the orthorhombic space group *Cmcm*: The M^{5+} ion is coordinated with six oxygen ions, forming a MO_6 octahedron. These octahedra share corners forming one-dimensional chains which are oriented along the c-axis. The same space group *Cmcm* has been applied for Ln_3RuO_7 (*Ln* = La ~ Gd) [2-13], Ln_3ReO_7 (*Ln* = Pr, Nd, Sm ~ Tb) [14-17], Ln_3OsO_7 (*Ln* =Pr, Nd, Sm ~ Gd) [11, 18-20], Ln_3TaO_7 (*Ln* = La ~ Nd) [21-25], Ln_3IrO_7 (*Ln* = Pr, Nd, Sm, Eu) [26-28], Pr_3NbO_7 [24] and Pr_3SbO_7 [24]. For Ln_3TaO_7 (*Ln* = Y, Sm ~ Ho) [21-23, 25], Ln_3SbO_7 (*Ln* = Y, Dy, Ho) [21, 29], Ln_3ReO_7 (Ln = Dy, Ho) [16, 17], and Gd_3NbO_7 [21], the space group $C222_1$ has been applied.

Due to this unique crystal structure and possible related magnetic properties, many studies have been performed, especially for the magnetic properties of compounds containing Ru^{5+} ion at the *M*-site because of its largest possible spin (S = 3/2) [2-12]. However, there was scant evidence for the expected one-dimensionality in the magnetic susceptibility.

Another topic for Ln_3MO_7 is that ruthenium-, iridium- and osmium containing members of the Ln_3MO_7 family show low-temperature structural phase transitions by detailed magnetic and thermal

investigations [8-10, 12, 13, 19, 20, 27, 30].

Now, we have paid our attention on the *M* = Sb compounds. Rossell determined the crystal structure of Y_2GdSbO_7 with the space group $C222_1$ [1]. Later, IJdo et al. determined the structure for Pr_3SbO_7 with the space group *Cmcm* [24]. Fennell et al. investigated the structure and magnetic properties of Ho_3SbO_7 and Dy_3SbO_7 [29]. They adopted the space group $C222_1$ for the two compounds. However, no atomic coordinates were presented for any of the compounds. We prepared a series of Ln_3SbO_7 compounds for all Ln ions, and determined their structures by X-ray diffraction measurements (for Ln = La and Pr, the space group is *Cmcm*, and for Ln = Sm-Lu, the space group $C222_1$ is applied) [31]. After that, Fu and IJdo presented an alternative setting of the *Cmcm* space group, i.e., *Ccmm* for Y_3SbO_7 [32]. Very recently, Siqueira et al. pointed out that the space group *Ccmm* is suitable for other Ln_3SbO_7 compounds with intermediate-sized Ln ions, from the second harmonic generation (SHG) and Raman scattering measurements [33].

In this study, we re-examined the structure and magnetic properties for Ln_3SbO_7 (*Ln* = La, Pr, Nd, Sm-Dy) compounds. After checking the existence of the phase transition in these compounds, we performed their high-temperature X-ray diffraction measurements in order to determine their structures above and below the phase transition temperatures. Through their magnetic susceptibility and specific heat measurements, we observed an antiferromagnetic transition at 3.0 K (*Ln* = Nd) and 7.8 K (*Ln* = Tb). Their results will be discussed in this paper.

2. Experimental

2.1. Sample preparation

As starting materials, rare earth oxides Ln_2O_3 (*Ln* = La, Nd, Sm-Gd, Dy), Pr_6O_{11}, Tb_4O_7, and Sb_2O_3 were used. For La_2O_3 and Nd_2O_3, they absorb moisture in air and easily form rare earth hydroxides $Ln(OH)_3$. Therefore, they were dried at 1173 K for 24 h before use. For better reactivity, mixtures of the rare earth oxides and Sb_2O_3 were dissolved in the conc. nitric acid, and were heated first at 423 K for one night and then at 873 K for 6 h. These mixtures were pressed into pellets and heated at 1473 K for 12 h. In the first stage of sample preparations, very small amounts of impurities remained in the desired compounds; they were un-reacted starting materials Ln_2O_3. In order to remove these impurities, the samples were washed with diluted hydrochloric acid. After this treatment, single-phase Ln_3SbO_7 compounds could be obtained.

2.2. X-ray diffraction analysis

Powder X-ray diffraction profiles were measured using a Rigaku Multi-Flex diffractometer with Cu-*Kα* radiation (λ = 1.5406 Å) equipped with a curved graphite monochromator. The data were collected by step-scanning in the angle range of $10° \leq 2\theta \leq 120°$ at a 2θ step-size of 0.02°. For Nd_3SbO_7 and Tb_3SbO_7, the temperature dependence of the X-ray diffraction profiles ($15° \leq 2\theta \leq 120°$) was obtained in the temperature range from 373 to 1123 K.

The X-ray diffraction data were analyzed by the Rietveld technique, using the programs RIETAN-FP [34], and the crystal structure was drawn by using the VESTA program [35].

2.3. Magnetic susceptibility measurements

The temperature-dependence of the magnetic susceptibility was measured in an applied field of 0.1 T over the temperature range of $1.8 \text{ K} \leq T \leq 400 \text{ K}$, using a SQUID magnetometer (Quantum Design, MPMS5S). The susceptibility measurements were performed under both zero-field-cooled

(ZFC) and field-cooled (FC) conditions. The former was measured upon heating the sample to 400 K under the applied magnetic field of 0.1 T after zero-field cooling to 1.8 K. The latter was measured upon cooling the sample from 400 to 1.8 K at 0.1 T.

2.4. Specific heat measurements

Specific heat measurements were performed using a relaxation technique by a commercial heat capacity measuring system (Quantum Design, PPMS) in the temperature range of 1.8-400 K. The sintered sample in the form of a pellet was mounted on a thin alumina plate with Apiezon for better thermal contact.

3. Results and discussion

3.1. Preparation and crystal structure

Figure 1 shows the powder X-ray diffraction profiles for Ln_3SbO_7 (*Ln* = La, Pr, Sm, Eu, Gd). Except for *Ln* = Nd, all the Ln_3SbO_7 compounds (*Ln* = La, Pr, Sm-Dy) were obtained as a single phase. These diffraction patterns are similar to that for the fluorite structure and all reflections appear to be consistent with the C-centered condition, $h + k = 2n$. Although a variety of space groups such as *Pnma*, *Cmcm*, $P2_12_12_1$, $C222_1$, *Ccmm*, $P2/n$ and $P2_1nb$ have been proposed for the Ln_3MO_7, the C-centering extinction condition ruled out space groups such as *Pnma*, $P2_12_12_1$, $P2/n$ and $P2_1nb$. For the diffraction profiles of La_3SbO_7 and Pr_3SbO_7, some extra reflection peaks which should be observed with space groups $C222_1$ and *Ccmm* (for example, the peak at $2\theta \sim 20.5°$ corresponding to the 2 0 1 reflection) were not observed in the X-ray diffraction profiles. This fact shows that the $C222_1$ and *Ccmm* were also ruled out from the space group for La_3SbO_7 and Pr_3SbO_7. We performed Rietveld refinements of the

crystal structure with the space group *Cmcm*. All the reflections observed could be successfully indexed. Figure 2 (a) shows the results of the Rietveld refinements for the X-ray diffraction profile of Pr_3SbO_7, and Table 1 lists the crystallographic data. A relatively large deviation of the unit cell parameters (*a*, *b*, *c*) with respect to the idealized ($2a_c$, $\sqrt{2}a_c$, $\sqrt{2}a_c$) cell derived from the cubic fluorite structure is noticed. Fig. 3 (a) illustrates the schematic crystal structure of Pr_3SbO_7. The SbO_6 octahedra are corner-linked through the O(3) atoms, and they form one-dimensional chains along the *c*-axis. One-third of the Pr atoms are in eight-fold oxygen coordination, forming distorted cubes $Pr(1)O_8$. These $Pr(1)O_8$ cubes are aligned one-dimensionally by edge sharing along the *c*-axis, which alternate with the parallel zigzag chains of SbO_6 octahedra, forming slabs parallel to the *b*-*c* plane. The remaining two-thirds of Pr(2) ions are in seven coordination and lie between the slabs of the $Pr(1)O_8$ and the SbO_6 polyhedra. Figures 3 (b) depicts the structure of Pr_3SbO_7 viewed along the *c*-axis.

For the X-ray diffraction profiles of Ln_3SbO_7 (*Ln* = Sm ~ Dy), some extra reflection peaks were observed (for example, the peak at $2\theta \sim 20.5°$ which is allowed in the space groups $C222_1$ and *Ccmm*). In addition, the X-ray diffraction profiles show the absence of the 0 *k l* reflections with $l = 2n+1$, e.g. the (0 2 1) reflection at 26.9°, which are allowed in the space group $C222_1$. This result means that the $C222_1$ is ruled out from the space group for these compounds. All the reflections observed could be successfully indexed with the space group *Ccmm*. Figure 2 (b) shows the results of the Rietveld refinements for the powder X-ray diffraction profile of Tb_3SbO_7. Table 2 lists the lattice parameters and atomic coordinates for Tb_3SbO_7. Figures 3 (c) shows the crystal structures of Tb_3SbO_7 viewed along the *c*-axis. The structure of Tb_3SbO_7 is similar to that of Pr_3SbO_7, because the space groups (*Ccmm* and *Cmcm*) are different settings of the same space group. In both structures (Pr_3SbO_7 and Tb_3SbO_7), the

chains of the MO_6 octahedra are parallel to the *c*-axis. The lanthanide ions are coordinated with seven and eight oxygens, respectively. The main difference is, however, the tilting of the MO_6 octahedra. In *Cmcm*, they tilt around the axes parallel to [1 0 0]; in *Ccmm*, they tilt around the [0 1 0] direction.

The X-ray diffraction profile for Nd_3SbO_7 is depicted in Fig. 2 (c). The Rietveld analysis for Nd_3SbO_7 shows that the phase with the space group *Cmcm* and that with *Ccmm* coexist at room temperature, and that the ratio of the C*mcm* phase and the C*cmm* phase is 48 %:52 %.

Figure 4 shows the variation of lattice parameters for Ln_3SbO_7 (Ln = La ~ Dy) against the ionic radius of the eight-coordinated Ln^{3+} ion. The lattice parameters increase with the ionic radius of Ln^{3+} and the differences among the $a/\sqrt{2}$, *b*, and *c* values become wide. The differences among $a/\sqrt{2}$, *b*, and *c* for the *Ccmm* phase are smaller than those for the *Cmcm* phase, indicating much smaller orthorhombic distortion in the *Ccmm* phase.

Figure 5 shows the variation of the average Ln-O and Sb-O bond lengths with the ionic radius of eight-coordinated Ln^{3+} ion. The average bond lengths Ln(1)-O and Ln(2)-O both increase with the ionic radius of Ln^{3+}. On the other hand, the average Sb-O bond lengths are nearly constant (~2.00 Å). This value is equal to the bond length calculated from the Shannon's ionic radii [36].

High temperature X-ray diffraction measurements for Nd_3SbO_7

The X-ray diffraction measurements for Nd_3SbO_7 show that the phase with the space group *Cmcm* and that with *Ccmm* coexist at room temperature. The Ln_3MO_7 compounds (M = Ru, Ir, Os, Ta) show structural phase transitions, and their high-temperature phases are known to have a space group *Cmcm*. Therefore, it is natural to consider that warming up Nd_3SbO_7 should transform into a single phase with

Cmcm space group.

Figure 6 shows the X-ray diffraction profiles of Nd_3SbO_7 at various temperatures. We performed the Rietveld analysis for the X-ray diffraction data assuming the two-phase model with space groups *Cmcm* and *Ccmm*. At room temperature, the ratio of the *Cmcm* phase and the *Ccmm* phase is determined to be 48 %: 52%. With increasing temperature, the ratio of the phase with the *Cmcm* space group increases, as listed in Table 3. The temperature range in which two phases coexist is very wide. The profiles above 873 K reveal that Nd_3SbO_7 transforms to a single phase with *Cmcm* space group.

Figure 7 shows the variation of the lattice parameters for Nd_3SbO_7 with temperature in the temperature range of 373 K ≤ T ≤ 923 K. The lattice parameters for both the phases (*Ccmm* and *Cmcm*) increase with temperature. No large change of the lattice parameters with varying temperature has been observed, which may be related to the fact that a two-phase region exists over a large temperature span.

High-temperature X-ray diffraction measurements were performed also for Tb_3SbO_7 in the temperature range between 373 K ≤ T ≤ 1123 K. The results showed that all the X-ray diffraction profiles collected in this temperature range were analyzed with the *Ccmm* model, i.e., no phase transition occurred.

3.2. Magnetic properties

For Nd_3SbO_7 and Tb_3SbO_7, magnetic susceptibility and specific heat measurements were performed in the temperature range between 1.8 and 400 K.

3.2.1. Magnetic properties of Nd_3SbO_7

Figure 8 shows the temperature dependence of the magnetic susceptibility for Nd_3SbO_7. The inset

shows its reciprocal susceptibility versus temperature curve and the Curie-Weiss fitting in the temperature range between 100 and 400 K. The effective magnetic moment of Nd_3SbO_7 is determined to be 6.33 μ_B. Therefore, the moment per mole of Nd^{3+} ion is 3.65 μ_B, which is close to the calculated moment for Nd^{3+} (3.62 μ_B). The negative Weiss constant of Nd_3SbO_7 (θ = -34.1 K) indicates that the magnetic interaction observed at low temperatures is antiferromagnetic.

A clear antiferromagnetic transition has been observed at 3.0 K (Fig. 8), and there is no divergence between the ZFC and FC susceptibilities below this temperature, which indicates that the Nd^{3+} ions are in an antiferromagnetic state without any ferromagnetic properties.

In order to obtain the information about the low-temperature magnetic behavior, specific heat measurements were performed down to 1.8 K. Figure 9 shows the temperature dependence of the specific heat (C_p) divided by temperature (C_p/T) for Nd_3SbO_7. A λ-type specific heat anomaly has been observed at 3.0 K, which corresponds to the results by magnetic susceptibility measurements. To evaluate the magnetic contribution to the specific heat (C_{mag}), we have to subtract the contribution of lattice specific heat (C_{lat}) from the total specific heat ($C_{mag} = C_p - C_{lat}$). The lattice specific heat was estimated by using the data for a diamagnetic compound La_3NbO_7 (the red solid line in Fig. 9). The magnetic specific heat below 1.8 K was extrapolated by the relation $C_{mag} \propto T^3$ from the spin-wave model for the antiferromagnet [37] (the dashed line in Fig. 9). From the temperature dependence of the magnetic specific heat, the magnetic entropy change for Nd_3SbO_7 (S_{mag}) is calculated by the relation $S_{mag} = \int (C_{mag}/T) dT$. Its temperature dependence is also shown in Fig. 9. The total magnetic entropy change is ~ 14 J/mol K, and this value is close to $3R \ln 2$ = 17.3 J/mol K (R: gas constant). The Nd^{3+} ions in the Nd_3SbO_7 occupy two crystallographic sites, the 8-coordinated Ln(1) site and 7-coordinated

Ln(2) site. In both the sites, the ground multiplet $^4I_{9/2}$ of the Nd^{3+} ion should split into five Kramers doublets due to the effect of the crystal field in the orthorhombic symmetry. At sufficiently low temperatures, only the lowest doublet of each Nd^{3+} ion needs to be considered. The experimental results indicate that the ground Kramers' doublets for three Nd^{3+} ions cause the antiferromagnetic ordering of Nd_3SbO_7.

3.2.2. Magnetic properties of Tb_3SbO_7

Figure 10 shows the temperature dependence of the magnetic susceptibility for Tb_3SbO_7. The inset shows the reciprocal susceptibility versus temperature curve and the Curie-Weiss fitting in the temperature range of 100 and 400 K. The effective magnetic moment of Tb_3SbO_7 is determined to be 16.81 μ_B. Therefore, the effective magnetic moment per mole of Tb^{3+} ion in Tb_3SbO_7 is 9.71 μ_B, which is close to the calculated moment for Tb^{3+} (9.72 μ_B). The negative Weiss constant of Tb_3SbO_7 (θ = -12.4 K) indicates that the magnetic interaction observed at low temperatures is antiferromagnetic.

An antiferromagnetic transition has been observed at 3.0 K, and there is no divergence between the ZFC and FC susceptibilities below this temperature.

Figure 11 shows the temperature dependence of the specific heat for Tb_3SbO_7. A clear λ-type specific heat anomaly has been observed at 3.0 K, at which the magnetic susceptibility shows antiferromagnetic behavior. Another specific heat anomaly has been also observed at 7.8 K. At this temperature, the susceptibility of Tb_3SbO_7 also shows anomalous behavior (see the low-temperature dependence of the susceptibility of Fig. 10). The magnetic specific heat was estimated by subtracting the contribution of the lattice specific heat from the total specific heat in the same way as is the case for

Nd_3SbO_7. The magnetic entropy change is calculated from the specific heat data by using the equation $S_{mag} = \int (C_{mag}/T)dT$, and it is obtained to be 17.5 J/mol K at 10 K. This value is in good agreement with the calculated value, 17.3 J/mol K. The Tb^{3+} ion is a non-Kramers ion, and its ground multiplet $^7F_6$ should split into many states by the crystal field. Among the combinations of the possibly degeneracy of the Tb^{3+} ion (for Tb(1) and Tb(2) sites), only Rln2 + 2Rln2 = 17.3 J/mol K (the degeneracy of the Tb(1) and Tb(2) is both two) is reasonable for the obtained S_{mag} value. Therefore, it is considered that non-Kramers doublets of Tb^{3+} ions at each site individually cause the antiferrromagnetic ordering. As shown in Fig. 11, it is difficult to divide the magnetic entropy data into two anomalies. However, considering the results that the peak value of C_{mag}/T at 3.0 K is about twice as large as that at 7.8 K, we believe that the antiferromagnetic transitions at 3.0 and 7.8 K are due to the magnetic interactions between Tb^{3+} ions occupying the Tb(2) and Tb(1) sites, respectively, because two-thirds of the Tb^{3+} ions are situated at the Tb(2) sites and one-third of the Tb^{3+} ions are situated at the Tb(1) sites. Similar "two-step" magnetic transitions have been found for Ln_3TaO_7 (*Ln* = Nd, Tb) [25] and Ln_3NbO_7 (*Ln* = Nd, Tb) [38].

Summary

Rare earth antimonates Ln_3SbO_7 (*Ln* = rare earths) crystallize in an orthorhombic superstructure of cubic fluorite. Nd_3SbO_7 and Tb_3SbO_7 showed an antiferromagnetic transiton at 3.0 K and 7.8 K, respectively. Specific heat measurements for Tb_3SbO_7 indicate that the antiferromagnetic ordering of the 8-coordinated Tb ions begins to occur at 7.8 K, and the 7-coordinated Tb ions magnetically order at a furthermore lower temperature of 3.0 K.

References

[1] H. J. Rossell, *J. Solid State Chem*., **27**, 115-122 (1979).

[2] F. P. F. van Berkel and D. J. W. IJdo, *Mater. Res. Bull*., **21**, 1103-1106 (1986).

[3] W. A. Groen, F. P. F. van Berkel, and D. J. W. IJdo, *Acta Crystallogr*. Sec. **C 43**, 2262-2264 (1986).

[4] A. Kahn-Harari, L. Mazerrolles, D. Michel, and F. Robert, *J. Solid State Chem*., **116**, 103-106 (1995).

[5] P. Khalifah, R. W. Erwin , J. W. Lynn, Q. Huang, B. Batlogg, and R. J. Cava, *Phys. Rev.*, **B 60**, 9573-9578 (1999).

[6] F. Wiss, N. P. Raju, A. S. Wills, and J. E. Greedan, *Inter. J. Inorg. Mater.*, **2**, 53-59 (2000).

[7] B.P.Bontchev, A.J.Jacobson, M.M.Gospodinov, V. Skumryev, V. N. Popov, B. Lorenz, R. L. Meng, A. P. Litvinchuk, and M.N. Iliev, *Phys. Rev*. **B. 62**, 12235-12240 (2000).

[8] D. Harada and Y. Hinatsu, *J. Solid State Chem*., **158**, 245-253 (2001).

[9] D. Harada, Y. Hinatsu, and Y. Ishii, *J. Phys.: Condens. Matter*, **13**, 10825-10836 (2001).

[10] D. Harada and Y. Hinatsu, *J. Solid State Chem*., **164**, 163-168 (2002).

[11] R. Lam, F. Wiss, and J. E. Greedan, *J. Solid State Chem.* **167**, 182-187 (2002).

[12] W. R. Gemmill, M. D. Smith, and H-C, zur Loye, *Inorg. Chem*., **43**, 4254-4261 (2004).

[13] N. Ishizawa, K. Hiraga, D. du Boulay, H. Hibino, T. Ida, and S. Oishi, *Acta Cryst*., **E62**, i13-i16 (2006).

[14] G. Wltschek, H. Paulus, I. Svoboda, H. Ehrenberg, and H. Fuess, *J.Solid State Chem*. **125**, 1-4 (1996).

[15] R. Lam, T. Langet, and J. E. Greedan, *J. Solid State Chem*. **171**, 317-323 (2002).

[16] Y. Hinatsu, M. Wakeshima, N. Kawabuchi, and N. Taira, *J. Alloys Compd*., **374**, 79-83 (2004).

[17] M. Wakeshima and Y. Hinatsu, *J. Solid State Chem*., **179**, 3575-3581 (2006).

[18] J. R. Plaisier, R. J. Drost, and D. J. W. IJdo, *J. Solid State Chem.* **169**, 189-198 (2002).

[19] W. R. Gemmill, M. D. Smith, Y. A. Mozharivsky, G. J. Miller, and H-C, zur Loye, *Inorg. Chem.*, **44**, 7047-7055 (2005).

[20] Y. Hinatsu and Y. Doi, *J. Solid State Chem.*, **198**, 176-185 (2013).

[21] J. G. Allpress and H. J. Rossell, *J. Solid State Chem*., **27**, 105-114 (1979).

[22] Y. Yokogawa, M. Yoshimura, and S. Somiya, *Mater. Res. Bull*., **22**, 1449-1456 (1987).

[23] Y. Yokogawa, M. Yoshimura, and S. Somiya, *Solid State Ionics*, **28**, 1250-1253 (1988).

[24] J. F. Vente, R. B. Helmholdt, and D. J. W. IJdo, *J. Solid State Chem*. **108**, 18-23 (1994).

[25] M. Wakeshima, H. Nishimine, and Y. Hinatsu, *J. Phys.: Condens. Matter*, **16**, 4103-4120 (2004).

[26] J. F. Vente and D. J. W. IJdo, *Mater. Res. Bull.*, **26**, 1255-1262 (1991).

[27] H. Nishimine, M. Wakeshima, and Y. Hinatsu, *J. Solid State Chem*., **177**, 739-744 (2004).

[28] Y. Hinatsu, Y. Doi, H. Nishimine, M. Wakeshima, and M. Sato, *J. Alloys Compd*., **488**, 541-545 (2009).

[29] T. Fennell, S. T. Bramwell, and M. A. Green, *Can. J. Phys.*, **79**, 1415-1419 (2001).

[30] H. Nishimine, M. Wakeshima, and Y. Hinatsu, *J. Solid State Chem*., **178**, 1221-1229 (2005).

[31] Y. Hinatsu, H. Ebisawa, and Y. Doi, *J. Solid State Chem.*, **182**, 1694-1699 (2009).

[32] W. T. Fu and D. J. W. IJdo, *J. Solid State Chem*., **182**, 2451-2455 (2009).

[33] K. P. F. Siqueira, R. M. Borges, E. Granado, L. M. Malard, A. M. de Paula, R. L. Moreira, E. M.

Bittar, and A. Dias, *J. Solid State Chem*., **203**, 326-332 (2013).

[34] F. Izumi and K. Momma, *Solid State Phenom.*, **130**, 15-20 (2007).

[35] K. Momma and F. Izumi, *Appl. Crystallogr*., **41**, 653-658 (2008).

[36] R. D. Shannon, *Acta Crystallogr.*, **A32**, 751-767 (1976).

[37] S. J. Joshua and A. P. Cracknell, *Phys. Letter*, **A28**, 562-563 (1969).

[38] Y. Doi, Y. Harada, and Y. Hinatsu, *J. Solid State Chem.*, **182**, 709-715 (2009).

Figure captions

Fig. 1 Powder X-ray diffraction profiles for Ln_3SbO_7 (Ln = La, Pr, Sm, Eu, Gd).

Fig. 2 (a) Powder X-ray diffraction profiles for Pr_3SbO_7. The calculated profiles based on the *Cmcm* model are shown on the top solid line. The vertical marks in the middle show positions calculated for Bragg reflections. The lower trace is a plot of the difference between calculated and observed intensities.

(b) Powder X-ray diffraction profiles for Tb_3SbO_7. The calculated profiles based on the *Ccmm* model are shown on the top solid line. The vertical marks in the middle show positions calculated for Bragg reflections. The lower trace is a plot of the difference between calculated and observed intensities.

(c) Powder X-ray diffraction profile for Nd_3SbO_7. The calculated profiles based on the two-phase model are shown on the top solid line. The upper vertical marks in the middle show positions calculated for Bragg reflections (based on space group *Ccmm*). The lower vertical marks show positions calculated for Bragg reflections (based on space group *Cmcm*). The lower trace is a plot of the difference between calculated and observed intensities.

Fig. 3 (a) Schematic crystal structure of Pr_3SbO_7. (b) Structure for Pr_3SbO_7 (space group: *Cmcm*) viewed along the *c*-axis. (c) Structure for Tb_3SbO_7 (space group: *Ccmm*) viewed along the *c*-axis.

Fig. 4 Variation of lattice parameters for Ln_3SbO_7 with ionic radius of Ln^{3+} in 8-coordination.

Fig. 5 Variation of Ln-O and Sb-O bond lengths with ionic radius of Ln^{3+} in 8-coordination.

Fig. 6 X-ray diffraction profiles of Nd_3SbO_7 at various temperatures.

Fig. 7 Variation of lattice parameters for both phases of Nd_3SbO_7 with temperature. Filled symbols are for the phase with *Cmcm* space group; open symbols are for the phase with *Ccmm* space group.

Fig. 8 Temperature dependence of the magnetic susceptibility for Nd_3SbO_7 between 1.8 and 100 K. The inset shows the temperature dependence of the reciprocal magnetic susceptibility for Nd_3SbO_7 in the temperature range between 1.8 and 400 K. The solid line is the Curie-Weiss fitting.

Fig. 9 Temperature dependence of the specific heat divided by temperature (C_p/T) and the magnetic entropy (S_{mag}) for Nd_3SbO_7. Blue circles are C_p/T data for Nd_3SbO_7. Red solid line is the C_p/T data for La_3NbO_7.

Fig.10 Temperature dependence of the magnetic susceptibility for Tb_3SbO_7 between 1.8 and 400 K. The inset shows the temperature dependence of the reciprocal magnetic susceptibility for Tb_3SbO_7. The solid line is the Curie-Weiss fitting.

Fig.11 Temperature dependence of the specific heat divided by temperature (C_p/T) and the magnetic entropy (S_{mag}) for Tb_3SbO_7. Blue circles are C_p/T data for Tb_3SbO_7. Red solid line is the C_p/T data for La_3NbO_7.

Table 1 Structural parameters for Pr_3SbO_7.

Atom	Site	*x*	*y*	*z*	*B* / Å^2 [a]
Pr(1)	4*a*	0	0	0	0.52(4)
Pr(2)	8*g*	0.228(1)	0.294(2)	1/4	0.52
Sb	4*b*	0	1/2	0	0.30(4)
O(1)	16*h*	0.125(1)	0.317 (1)	–0.033(1)	1.2(1)
O(2)	8*g*	0.135(2)	0.021(2)	1/4	1.2
O(3)	4*c*	0	0.427(2)	1/4	1.2

Note. Space group *Cmcm*; a = 10.9578(10) Å, b = 7.5291(6) Å, c = 7.6593(6) Å, V = 631.91(9) Å^3, R_{wp} = 11.65 %, R_I = 2.82 %, and R_e = 8.62 %, where

$$R_{wp} = \left[\sum_i w_i \left(y_i - f_i(x)\right)^2 / \sum_i w_i {y_i}^2 \right]^{1/2}, \quad R_I = \sum \left| I_k(o) - I_k(c) \right| / \sum I_k(o), \text{ and}$$

$$R_e = \left[(N - P) / \sum_i w_i {y_i}^2 \right]^{1/2}.$$

Table 2 Structural parameters for Tb_3SbO_7.

Atom	Site	*x*	*y*	*z*	*B* / Å^2 [a]
Tb(1)	4b	0	0.5	0	0.49(6)
Tb(2)	8g	0.237(2)	0.237(2)	1/4	0.49
Sb	4a	0	0	0.007	0.29(4)
O(1)	16h	0.130(2)	0.202 (3)	-0.029(1)	1.2(1)
O(2)	4c	0.054(2)	0	1/4	1.2
O(3)	4c	0.118(3)	1/2	1/4	1.2
O(4)	4c	-0.127(3)	1/2	1/4	1.2

Note. Space group *Ccmm*; a = 10.5643(9) Å, b = 7.4766(8) Å, c = 7.5106(7) Å, V = 593.12(10) Å^3, R_{wp} = 10.24 %, R_I = 2.53 %, and R_e = 7.72 %.

Table 3 The ratio of *Cmcm* and *Ccmm* phases in Tb_3SbO_7 at various temperatures.

Temperature (K)	*Cmcm* (%)	*Ccmm* (%)
373	48	52
473	48	52
573	52	52
673	56	44
773	79	21
873	100	0
973	100	0

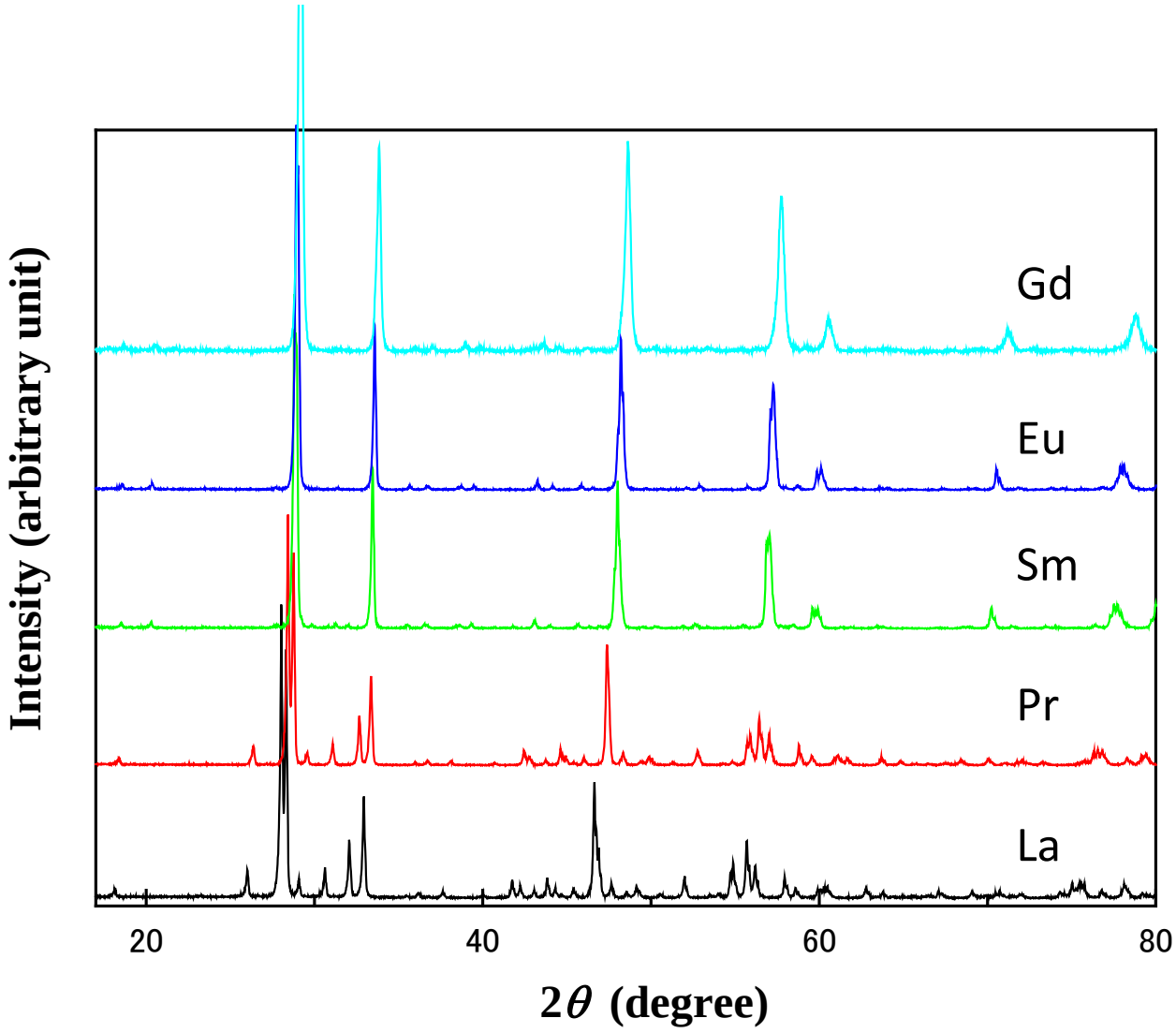

Fig.1

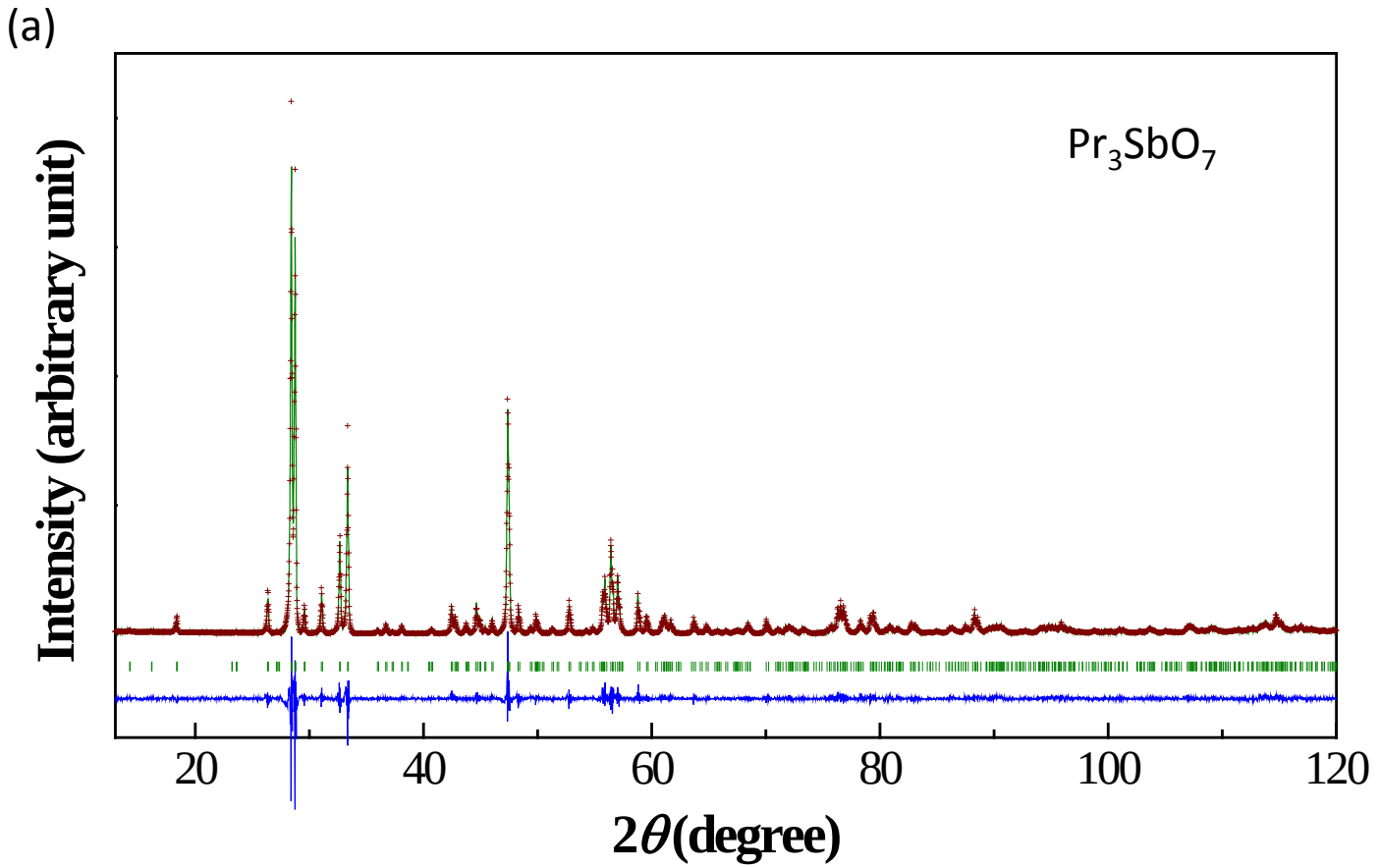
(a)
Intensity (arbitrary unit)
Pr3SbO7
20
40
60
80
100
120
2θ(degree)

Fig.2(a)

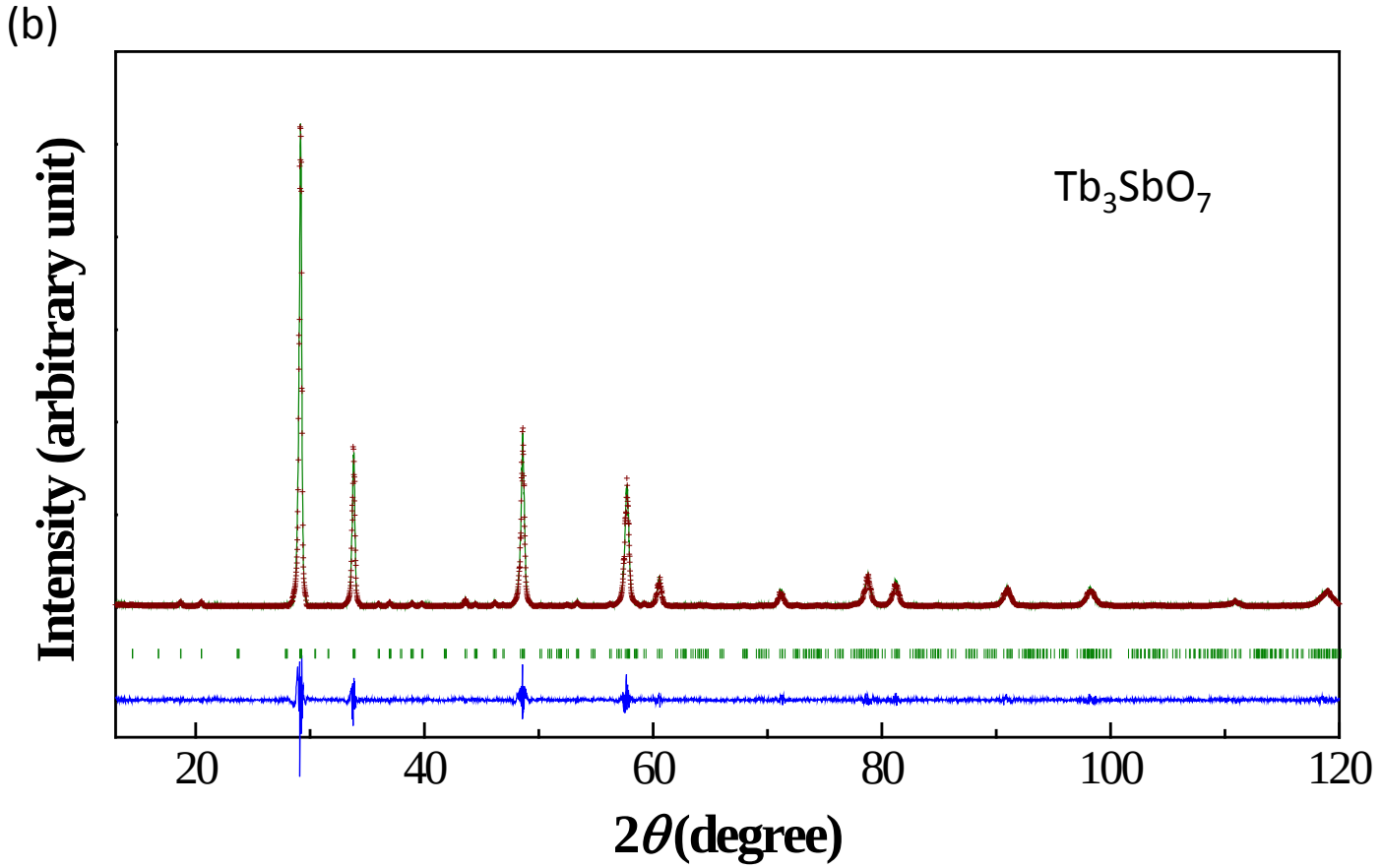
(b)
Intensity (arbitrary unit)
Tb3SbO7
20
40
60
80
100
120
2θ(degree)

Fig.2(b)

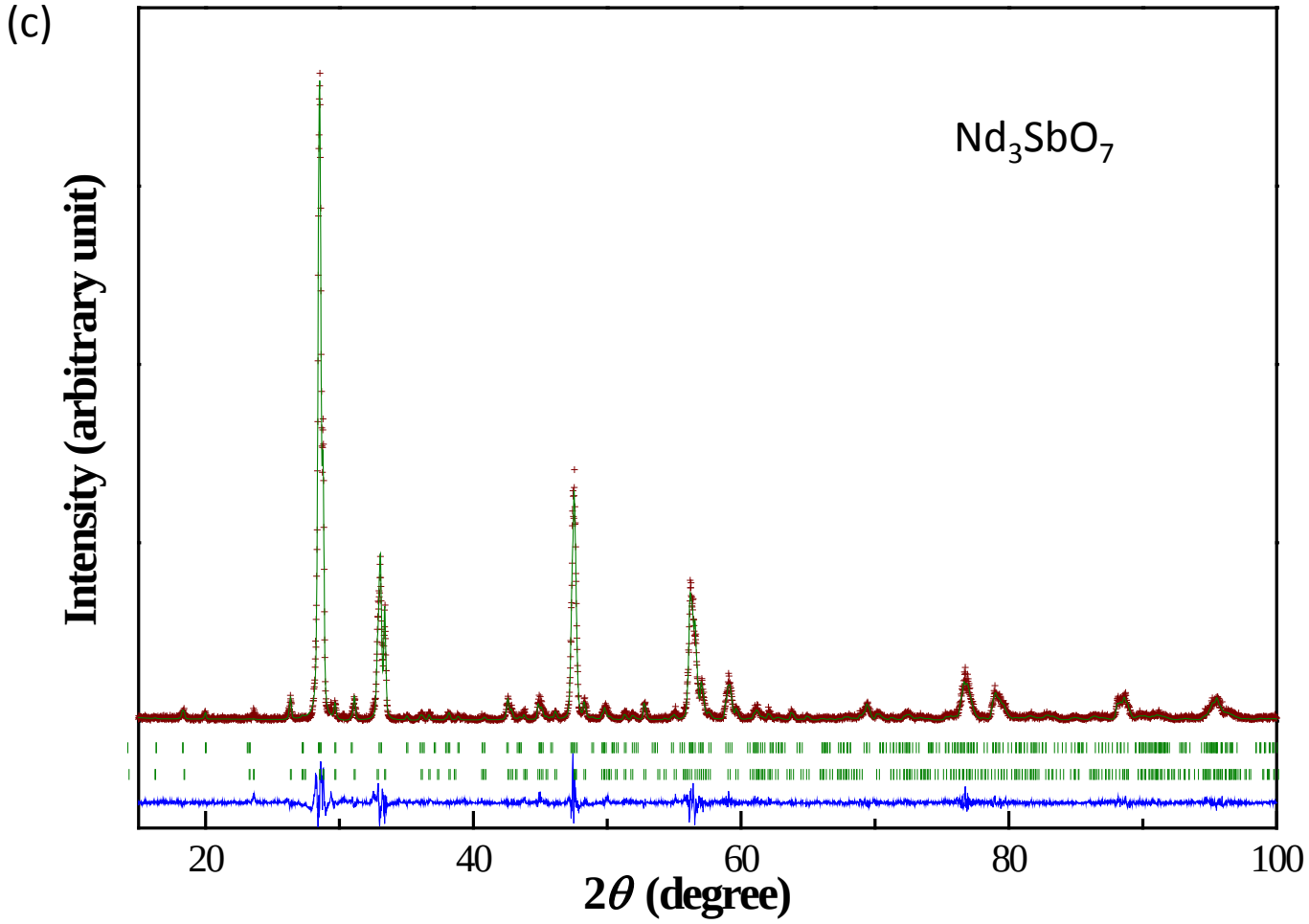

Fig. 2 (c)

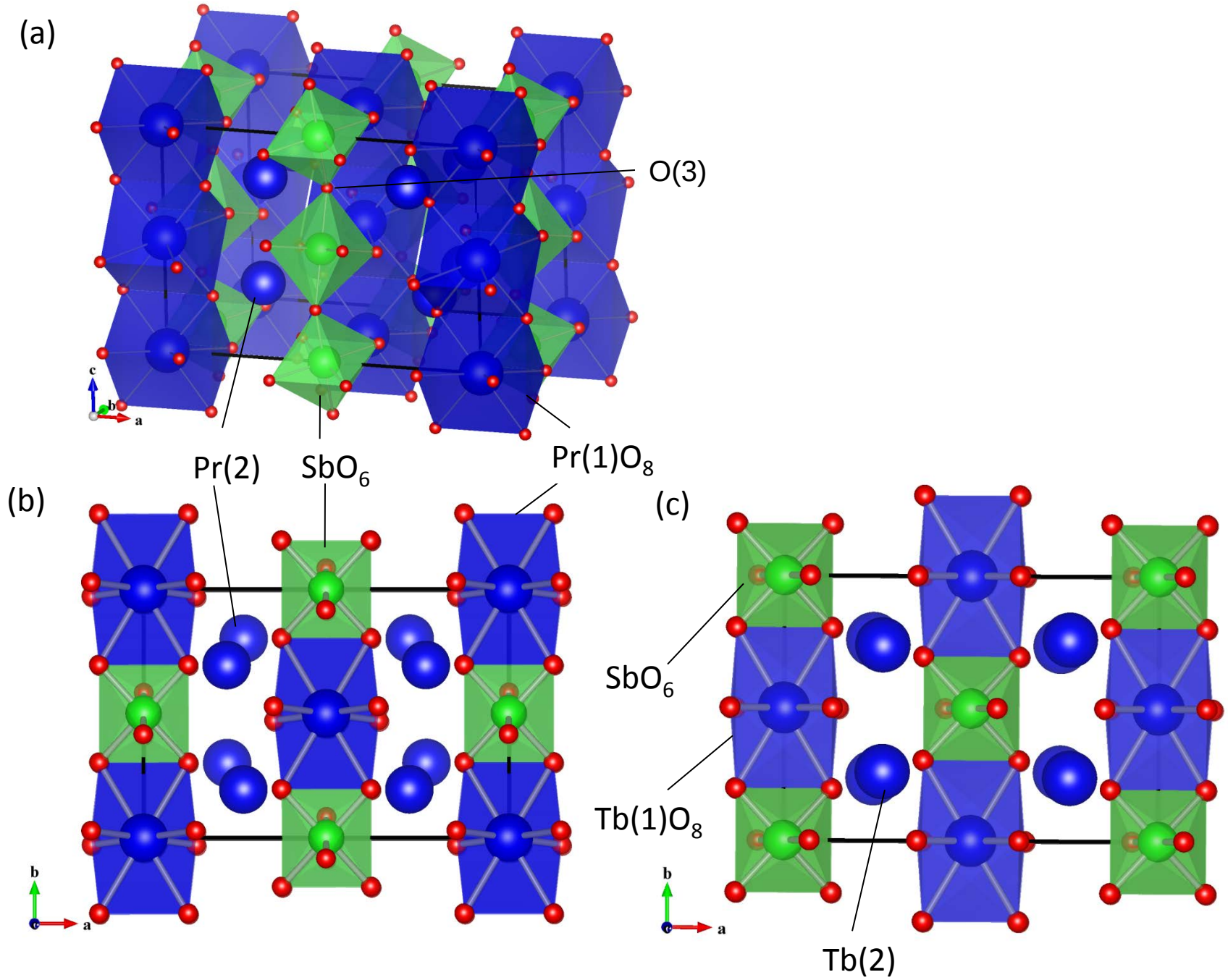

Fig.3

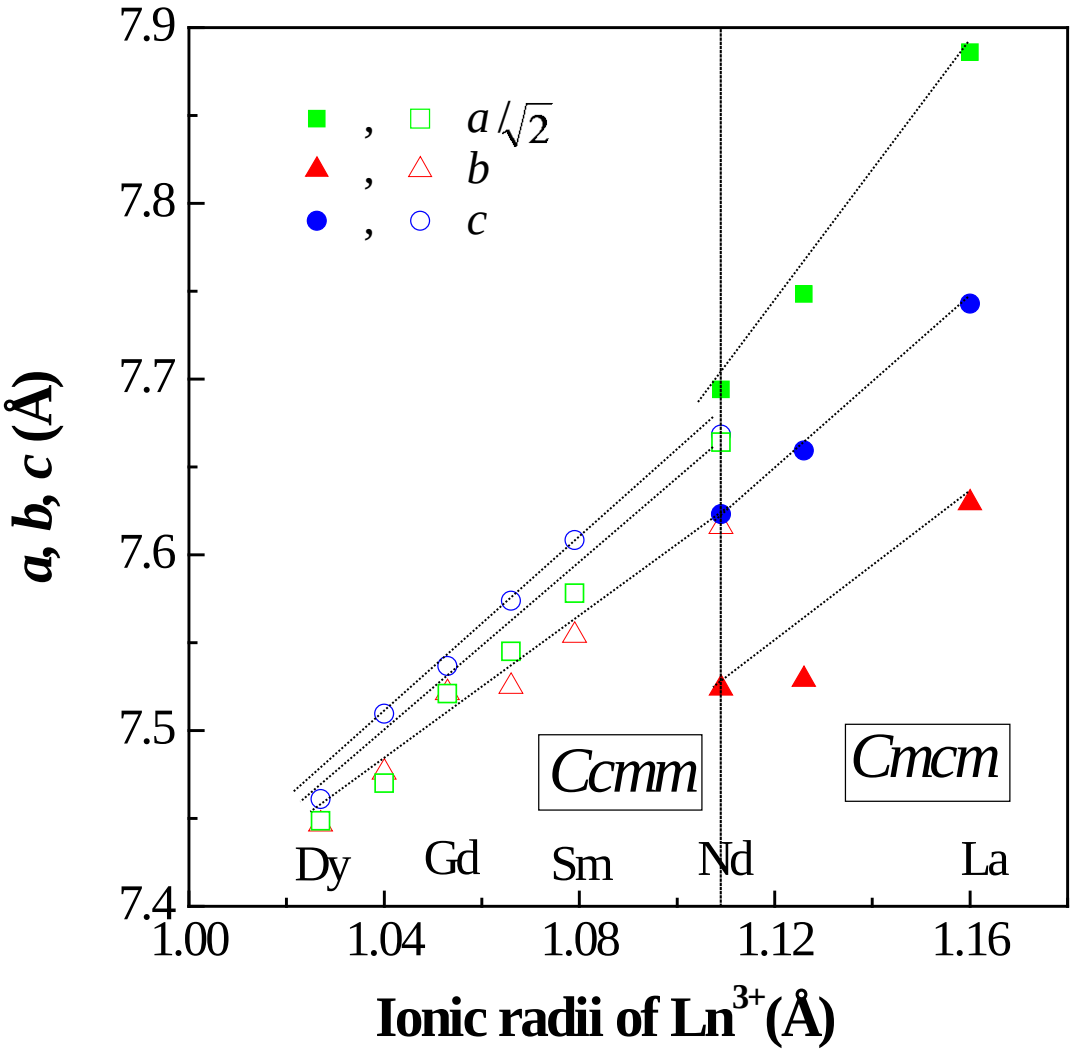
7.9
7.8
7.7
7.6
7.5
7.4
a, b, c (Å)
a/√2
b
c
Ccmm
Cmcm
Dy
Gd
Sm
Nd
La
1.00
1.04
1.08
1.12
1.16
Ionic radii of Ln3+(Å)

Fig.4

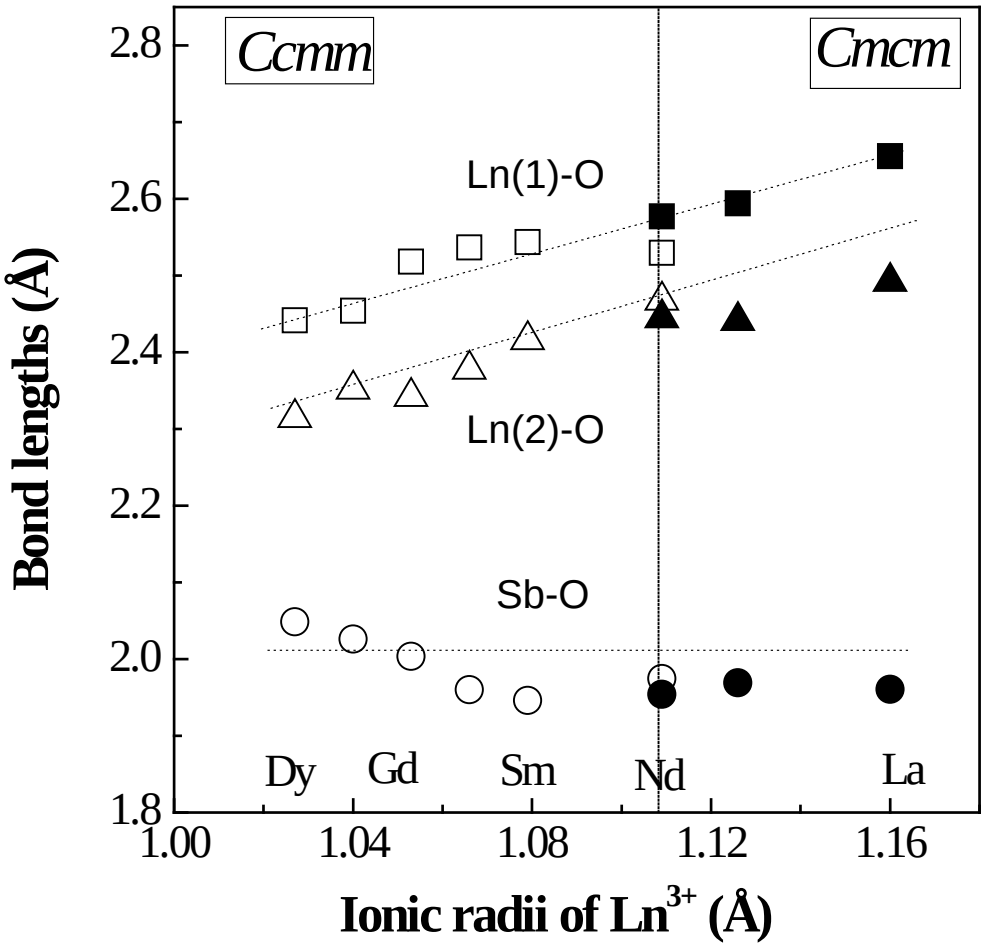
Ccmm
Cmcm
Ln(1)-O
Ln(2)-O
Sb-O
Dy
Gd
Sm
Nd
La
2.8
2.6
2.4
2.2
2.0
1.8
1.00
1.04
1.08
1.12
1.16
Bond lengths (Å)
Ionic radii of Ln3+ (Å)

Fig.5

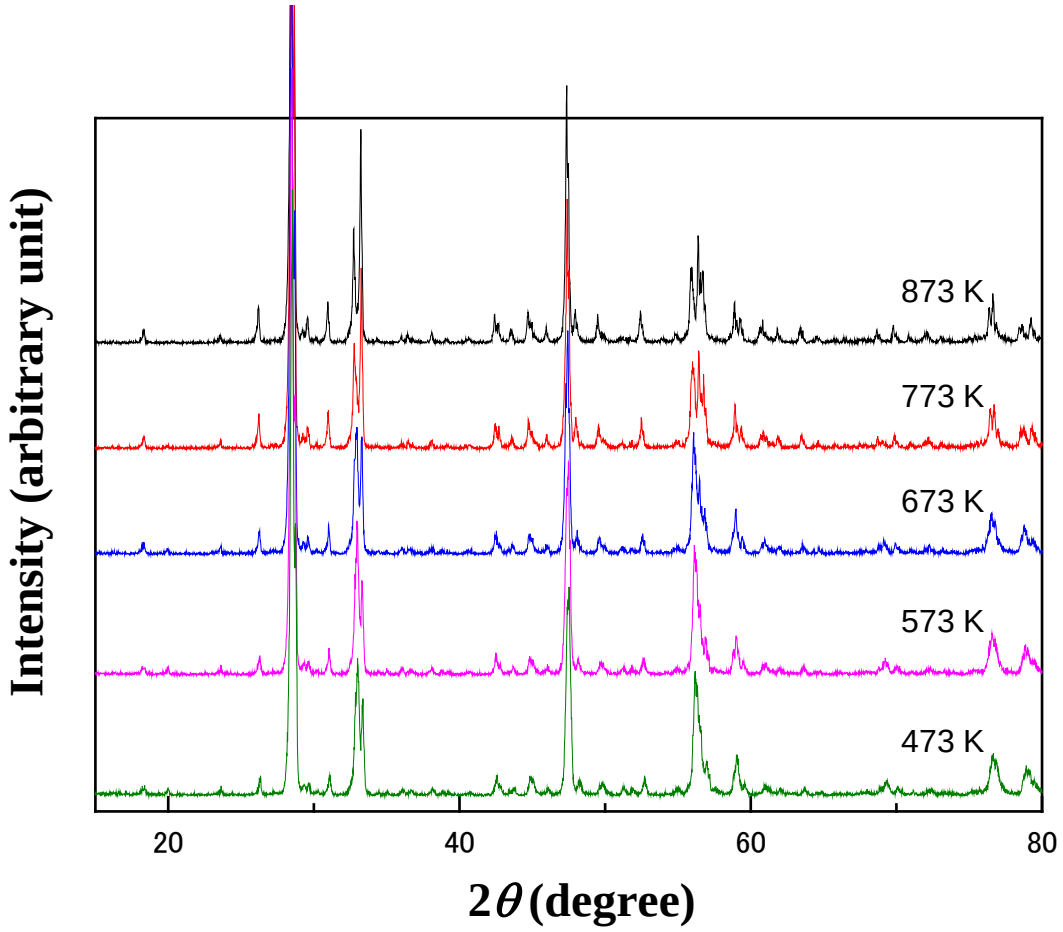
Intensity (arbitrary unit)
873 K
773 K
673 K
573 K
473 K
20
40
60
80
2θ (degree)

Fig.6

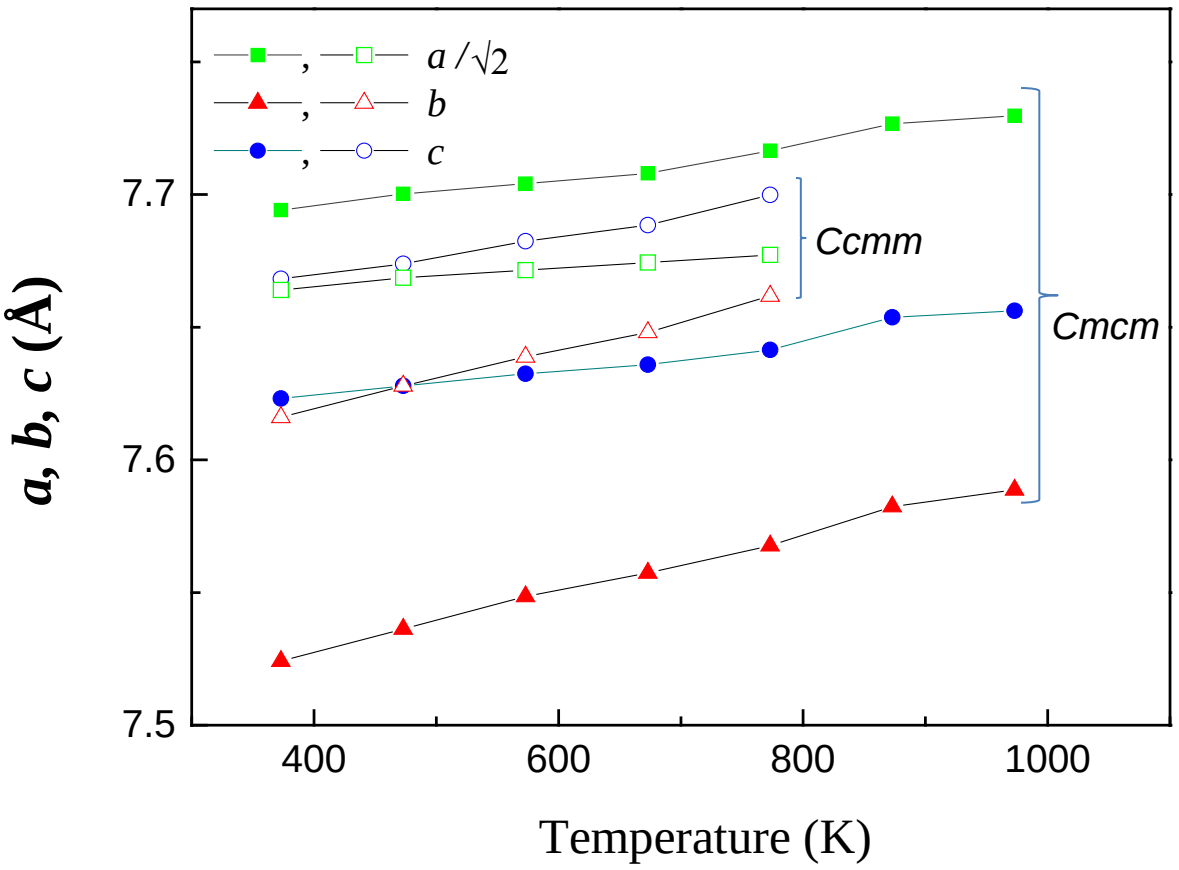

Fig.7

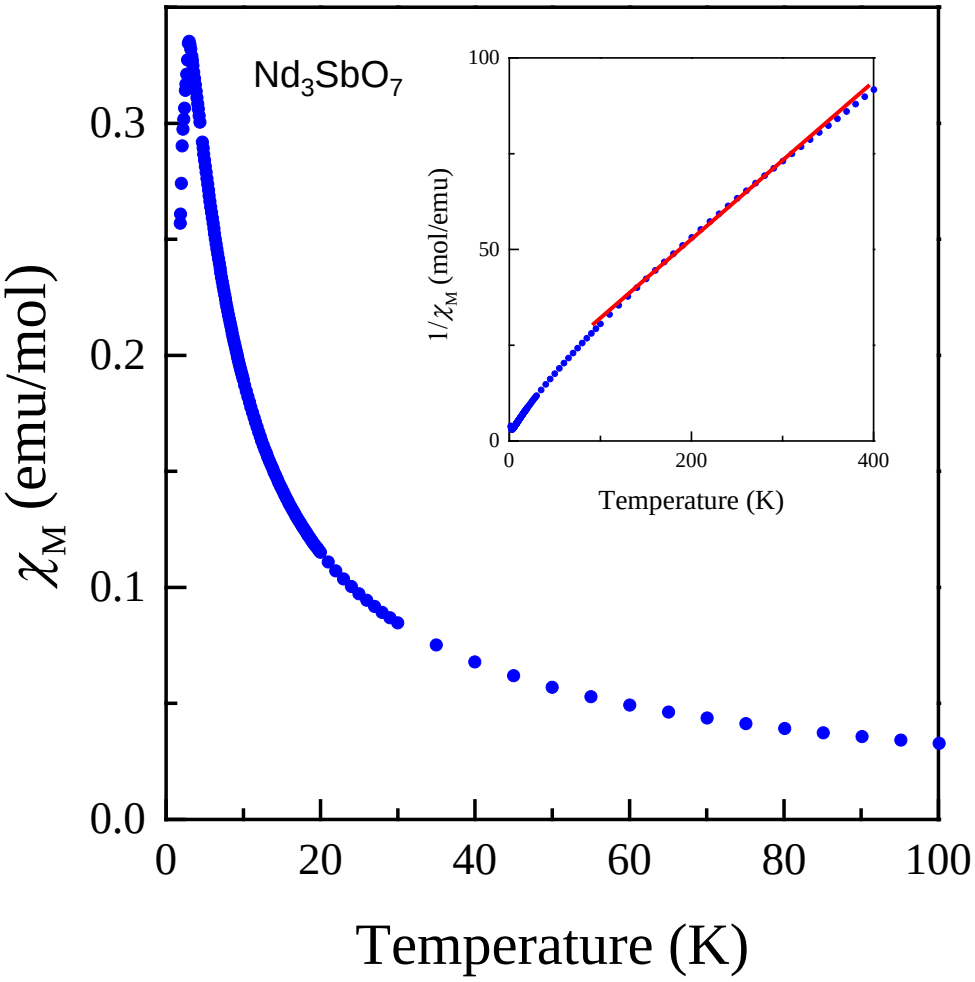
Nd3SbO7
χM (emu/mol)
0.0
0.1
0.2
0.3
0
20
40
60
80
100
Temperature (K)
1/χM (mol/emu)
0
50
100
0
200
400
Temperature (K)

Fig.8

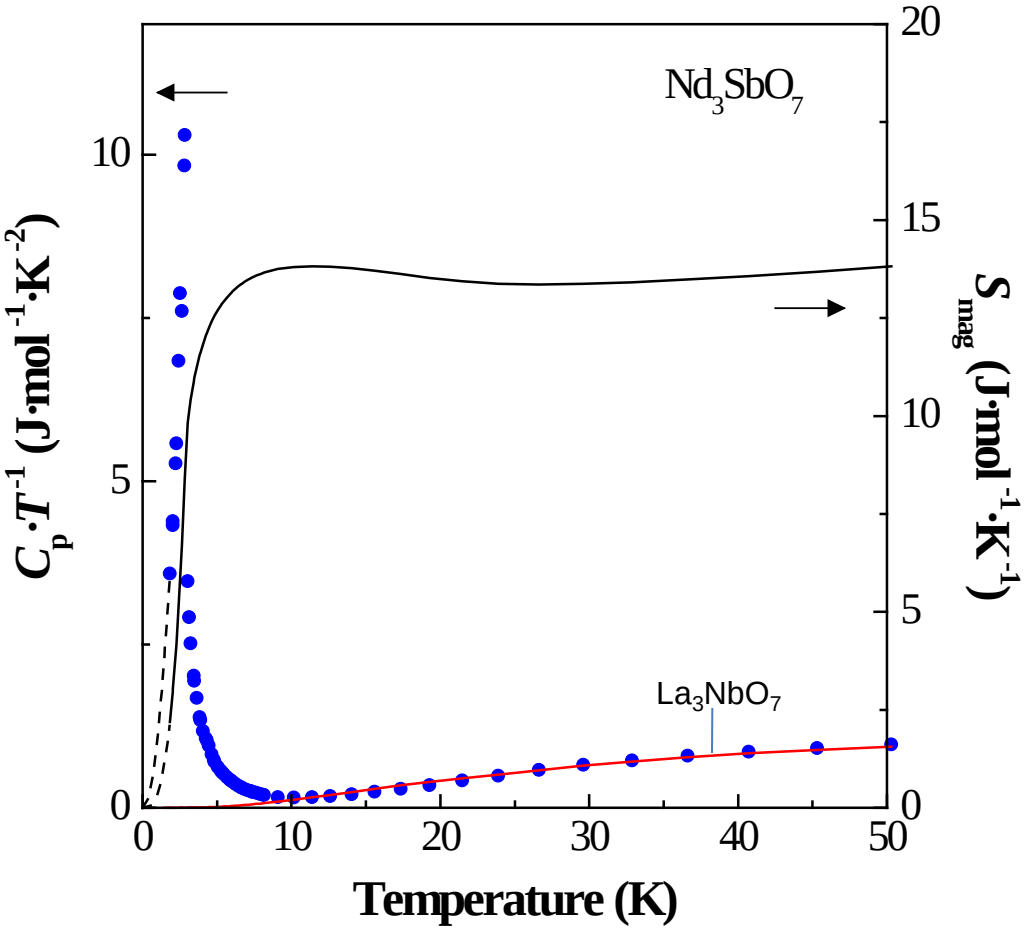
Nd3SbO7
La3NbO7
Cp·T-1 (J·mol-1·K-2)
Smag (J·mol-1·K-1)
Temperature (K)
0
5
10
0
5
10
15
20
0
10
20
30
40
50

Fig. 9

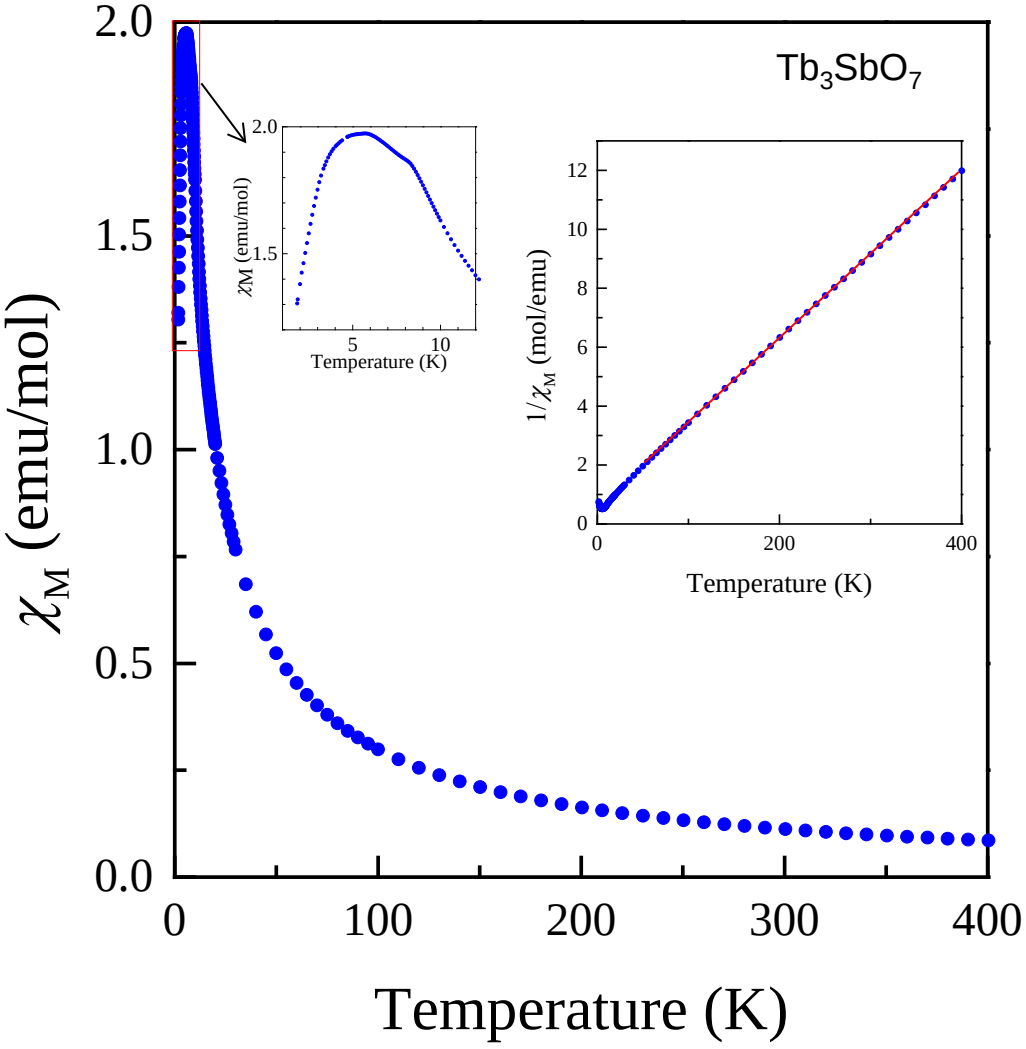
Tb3SbO7
χM (emu/mol)
Temperature (K)
2.0
1.5
1.0
0.5
0.0
0
100
200
300
400
χM (emu/mol)
Temperature (K)
1/χM (mol/emu)
Temperature (K)

Fig. 10

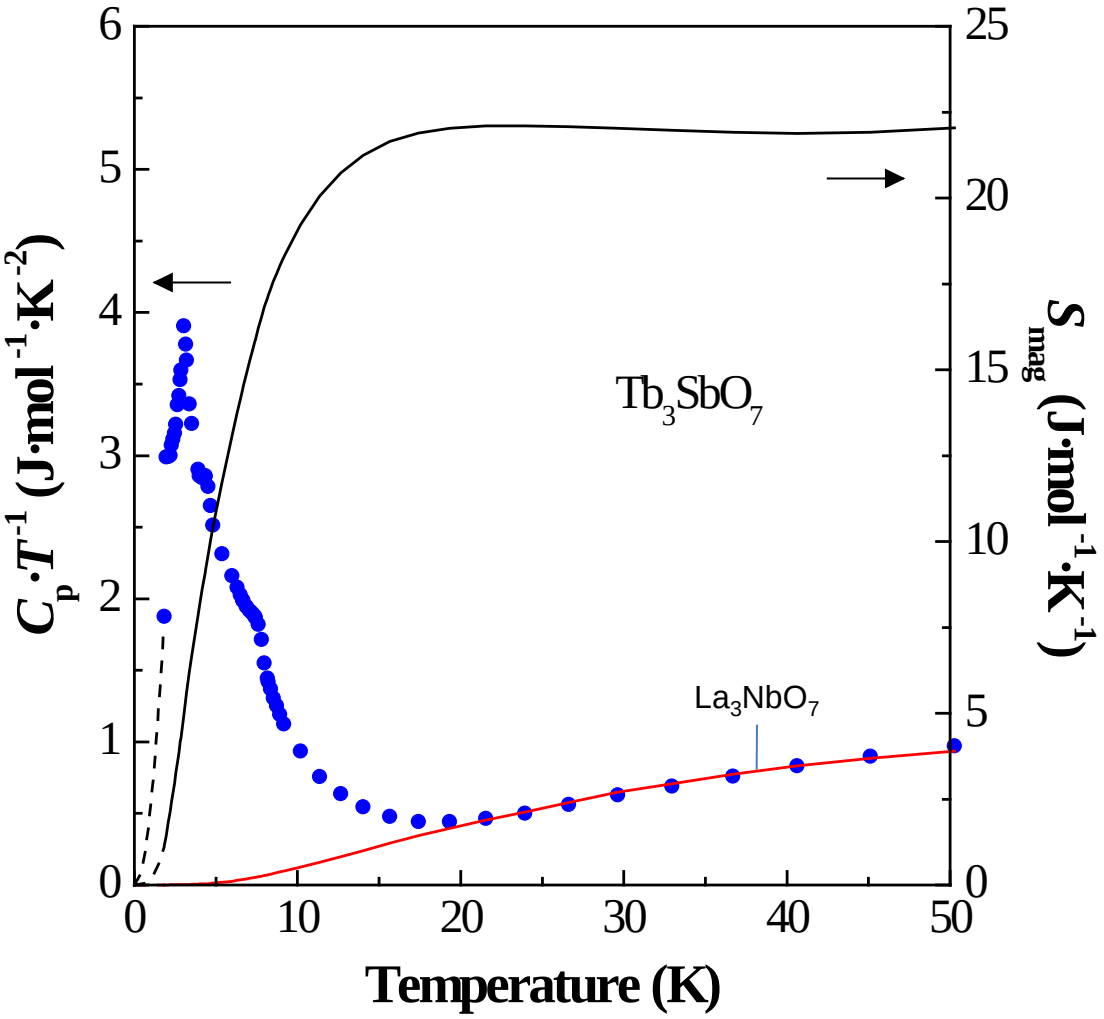
$C_p \cdot T^{-1}$ (J·mol^{-1}·K^{-2})
S_{mag} (J·mol^{-1}·K^{-1})
Temperature (K)
Tb_3SbO_7
La_3NbO_7
0
1
2
3
4
5
6
0
5
10
15
20
25
0
10
20
30
40
50

Fig.11